Robust reconfigurable modular metamaterials with demand-driven elasto-plastic properties

Haokai Zheng, Chunlei Li*, Zitong Feng, Qiang Han, Xiaohu Yao*

Department of Engineering Mechanics, School of Civil Engineering and Transportation, South China University of Technology, Guangzhou, Guangdong Province, 510640, P.R.China.

S1 Model design

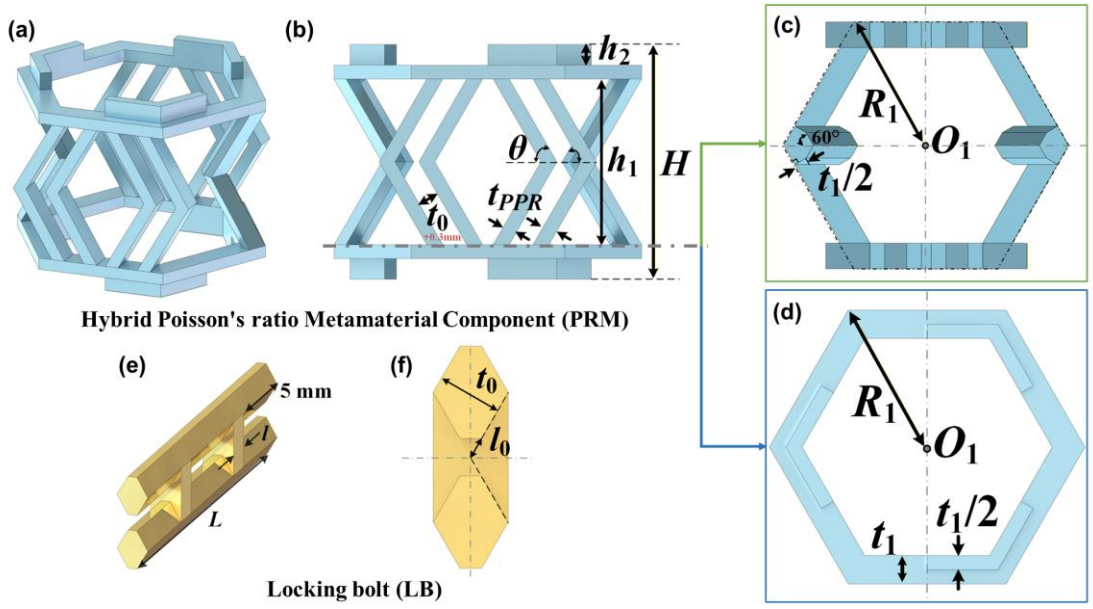

Figure S1 Geometric diagrams of (a)-(d) the PRM component and (e)-(f) the LB component

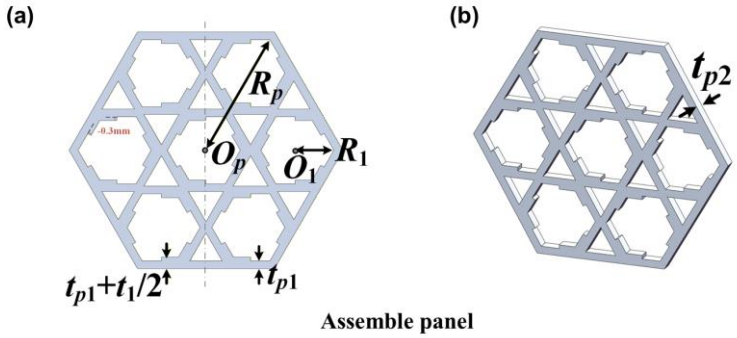

Figure S2 Geometric diagrams of the assemble panel

Figure S1 shows the geometric schematic diagrams of the PRM and LB components. The PRM component is with total height H and the circumscribed circle radius of the hexagonal cross-section midface R_1, the vertical span length of the positive Poisson's ratio beams (PPR) and negative Poisson's ratio beams (NPR) h_1, the mid-span folding angle θ, the thickness of PPR beams t_{PPR}, and the distance between the two adjacent PPR beams t_0. The LB component is with the length L, the thickness of the reinforcing ribs l, and the the length of the chamfer on the cross-section l_0. The cross-sectional thickness is the same as the distance t_0 between the two adjacent PPR beams. Figure S2 shows the geometric schematic diagrams of the assemble panel components. The panel is with the circumcircle radius R_p, outer wall thickness t_{p1} and out-of-plane thickness t_{p2}. The values of these parameters are in Table S1.

Table S1 Geometrical parameters

Parameters	Values	Parameters	Values
Total height of PRM H	17 mm	LB Length L	19.32 mm
Hexagonal cross-section midface radius of PRM R_1	10 mm	Thickness of reinforcing ribs l	1.5 mm
Vertical span length of PPR/NPR beams h_1	12 mm	Length of cross-section chamfer l_0	0.5 mm
Mid-span folding angle of PPR/NPR beams θ	60°	Circumcircle radius of panel R_p	66 mm
Thickness of PPR beams t_{PPR}	1 mm	Outer wall thickness of panel t_{p1}	2 mm
Distance between adjacent PPR beams t_0	1.5 mm	Out-of-plane thickness of panel t_{p2}	3 mm

S2 Specimen manufacturing and material property

S2.1 Specimen manufacturing

This study employed Selective Laser Melting (SLM) additive manufacturing technology to shape components, with printing equipment provided by Guangdong Hanbang 3D Tech Co., Ltd., model HBD-280. The base material for the components was aluminum alloy 6061, a heat-treatable alloy known for its excellent formability and machinability. The powder composition of the base material is detailed in Table S2.

Table S2 Composition of Al-6061 powder

	Al	Si	Mg	Fe	Cu	Mn	Ni	Ti	Zn	Pb	Sn
wt%	bal	0.3-0.7	0.35-0.8	≤0.5	≤0.1	≤0.03	≤0.05	≤0.01	≤0.01	≤0.01	≤0.01

The PRM, LB, and assemble panel components manufactured by 3D printing are shown in Figure S3. The printing direction of the SLM process is indicated by the orange arrow. Electron microscopy was used to examine the surface printing quality of the specimens. As shown in Figure S3(b) and (c), two key connection positions of the PRM component are locally magnified. The image reveals that the specimen is well printed, with no obvious defects, though some metal powder adheres to the surface. Consequently, a fault-tolerant assembly space of ±0.3 mm is reserved for the PRM

components (t_0+0.3mm) and the assemble panel, see the red markings in Figures S1 and S2.

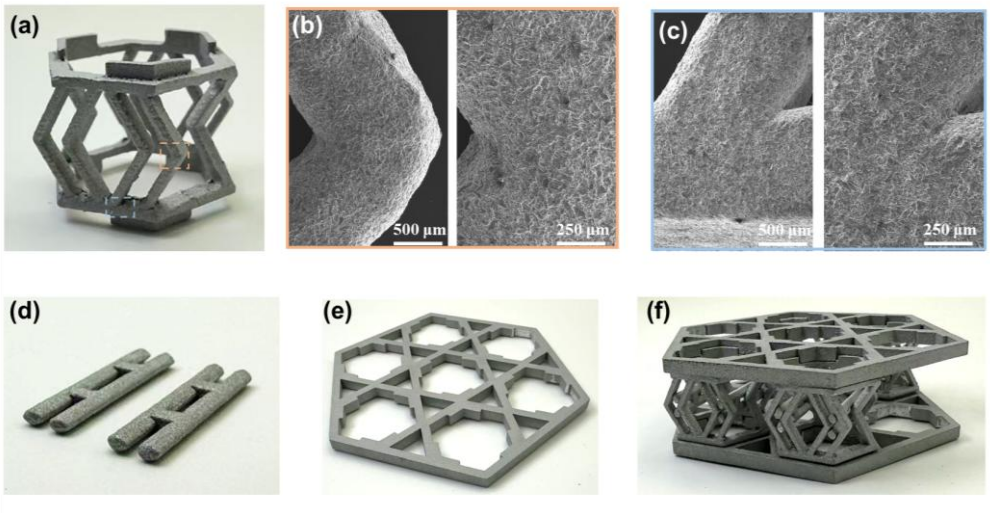

Figure S3 specimen of (a) PRM, (b) and (c) electron microscope image of PRM, (d) LB, (e) assemble panel and (f) RMMM-4mix structure.

Dynamic material models that account for strain hardening and strain rate have been developed to describe the plastic behavior of materials. Plastic deformation in metallic materials is generally attributed to the movement of dislocations within the metal lattice. However, as deformation progresses, metallic materials typically exhibit strain hardening. This phenomenon arises because the increasing resistance to dislocation motion causes the generation of new dislocations to plateau, thereby requiring higher loads to sustain further plastic deformation. To characterize this behavior, G. R. Johnson and W. H. Cook[1] proposed the Johnson–Cook plasticity model in the 1980s, which describes the flow stress of metallic materials by incorporating the effects of strain hardening, strain rate, and thermal softening, as expressed in Eq.(1)

$$\sigma_p = \left(A + B\varepsilon_p^n\right)\left[1 + C\ln\left(\frac{\dot{\varepsilon}}{\dot{\varepsilon}_r}\right)\right]\left(1 - T^*\right)^m \tag{1}$$

where, σ_p represents the plastic stress, A represents the initial yield stress, B is the strain hardening coefficient, n is the strain hardening exponent, ε represents the equivalent plastic strain, $\dot{\varepsilon}$ is the strain rate, $\dot{\varepsilon}_r$ is the reference strain rate, T^* is the dimensionless temperature term, m denotes the thermal softening exponent. In this study, all

experiments were conducted at room temperature and the temperature effect was not considered, Eq.(1) can be simplified as

$$\sigma_p = \left(A + B\varepsilon_p^n\right)\left[1 + C\ln\left(\frac{\dot{\varepsilon}}{\dot{\varepsilon}_r}\right)\right] \tag{2}$$

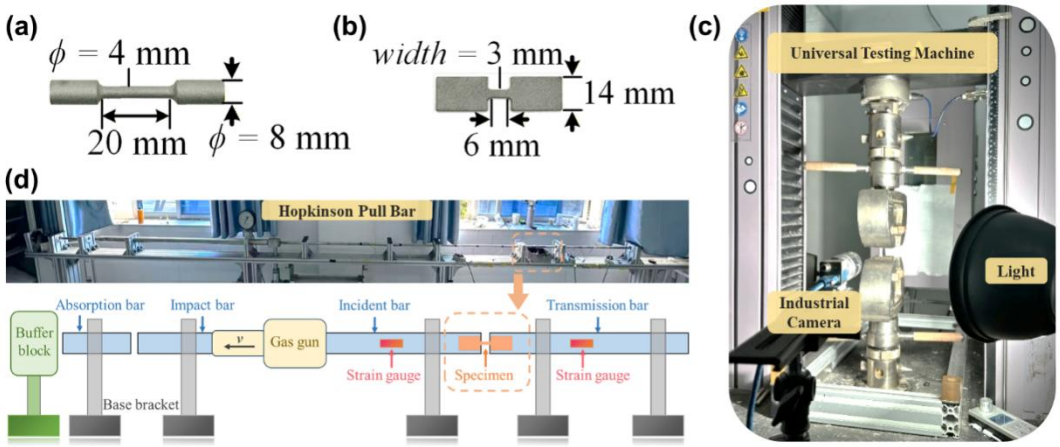

Figure S4 Dumbbell-shaped tensile specimens for (a) Quasi-static tensile and and (b) Hopkinson pull bar experiments; (c) uniaxial tensile experiments; (d) hopkinson pull bar experiments

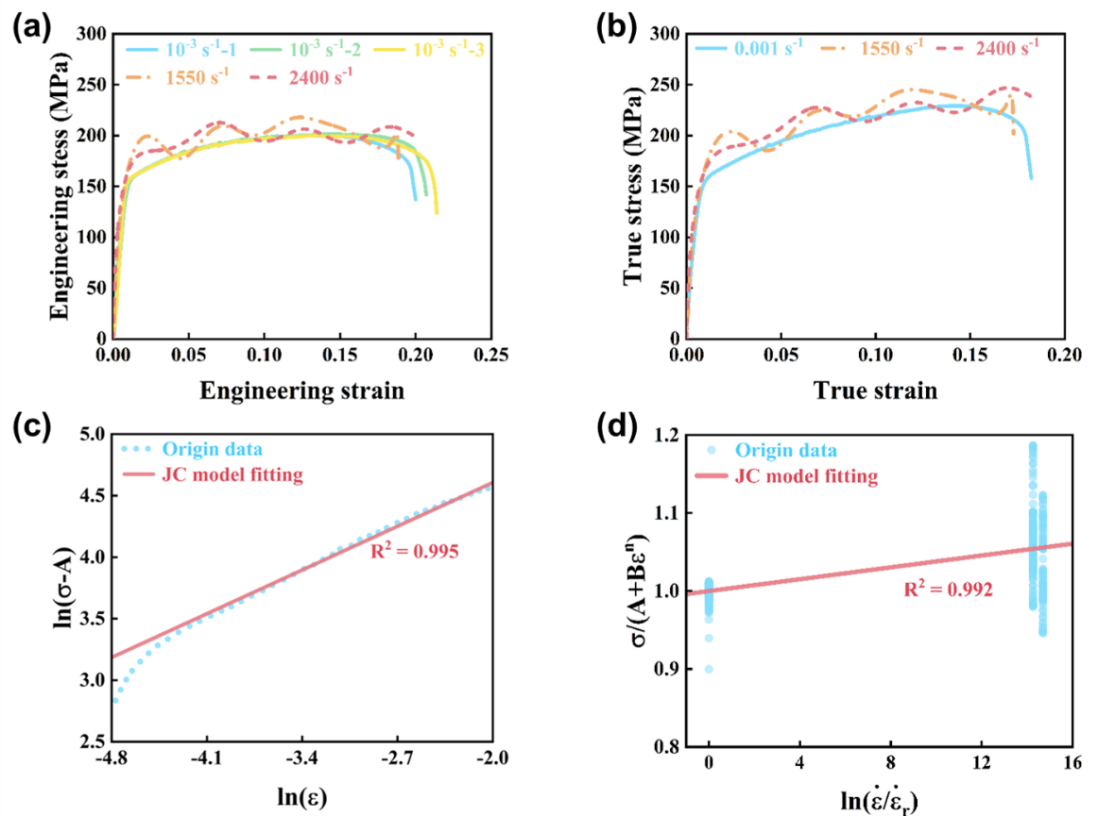

Figure S5 (a) Engineering stress-strain curves and (b) true stress-strain curves of 0.001 s^{-1}, 1500 s^{-1} and 2400 s^{-1} strain rates; (c) and (d) Johnson-Cook parameters fitting curves

As shown in Fig.S4 (c) and (d), to determine the parameters of the Johnson–Cook model, both quasi-static and dynamic tensile tests were conducted using a universal testing machine and split Hopkinson pull bar, respectively. For the quasi-static tensile tests, cylindrical specimens were prepared in accordance with ASTM E8/E8M, with a gauge length of 20 mm. The tensile speed was set to 1.2 mm/min, corresponding to a strain rate of 0.001 s^{-1}, to obtain the stress–strain data. Fig.S4 (d) illustrates the experimental facility of the pneumatic Hopkinson pull bar. The gauge length section of the dumbbell-shaped specimen used for dynamic testing has dimensions of 6 mm in length, 3 mm in width, and 1 mm in thickness. Experiments were conducted at air pressures of 0.24 MPa and 0.36 MPa, achieving strain rates of 1550 s^{-1} and 2400 s^{-1}, respectively. The dynamic data obtained were processed using the three-wave method to calculate stress, strain, and strain rate.

The engineering stress-strain data obtained from both quasi-static and dynamic tensile tests were transformed into true stress-strain curves, as shown in Fig.S5(a). Then, convert the engineering stress-strain curves into the true stress-strain curves according to Eq.(3) and (4), as shown in Fig.S5 (b).

$$\sigma = \sigma_{Eng}\left(1+\varepsilon_{Eng}\right) \tag{3}$$

$$\varepsilon = \ln\left(1+\varepsilon_{Eng}\right) \tag{4}$$

where σ and ε represents the true stress and strain, σ_{Eng} and ε_{Eng} represents the engineering stress and strain.

Under quasi-static conditions, the initial yield point of the stress-strain curve corresponds to the constant A, and Eq.(2) is subsequently transformed into Eq.(5). The values of parameters B and n are then determined, as depicted in Fig.S5 (c).

$$\ln\left(\sigma - A\right) = \ln B + n\ln\varepsilon \tag{5}$$

After the values of constants A, B, and n have been determined, Eq.(2) can be modified to Eq.(6). As shown in Fig.S5 (d), three sets of true strain-stress data with different strain rates (0.001 s^{-1}, 1550 s^{-1} and 2400 s^{-1}) were used to fit the parameter C. The material model parameters of aluminum alloy 6061 are listed in Table.1.

$$\frac{\sigma}{\left(A+B\varepsilon^{n}\right)}=\left(1+C\ln\frac{\dot{\varepsilon}}{\dot{\varepsilon}_{r}}\right) \tag{6}$$

S3 Quasi-static compression test and simulation

S3.1 Quasi-static compression test

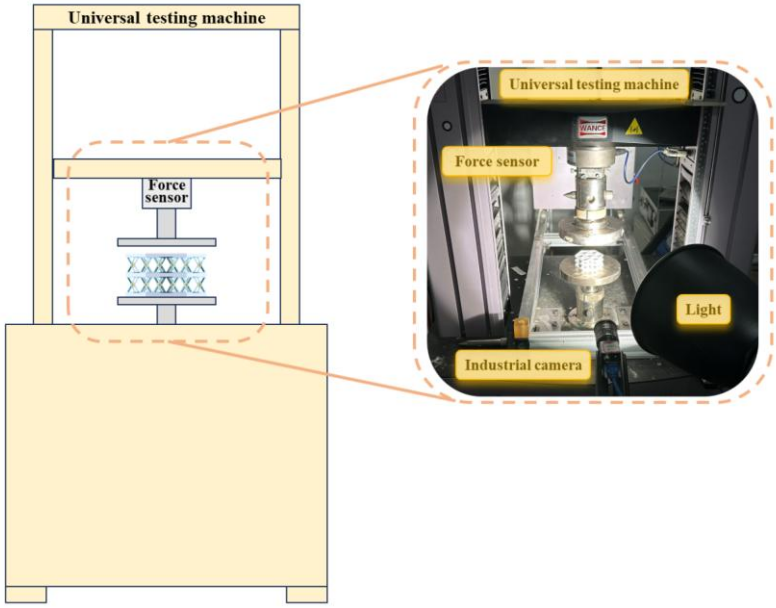

Figure S6 Quasi-static compression test

To investigate the compressive behavior and performance of the RMMM structures, quasi-static compressive experiments are performed by the WANCE universal testing machine, following the standard ASTM C365/C365M-22. As shown in Figure S6, a Daheng industrial camera is used to record the deformation of the structure. For the single-layer and double-layer RMMM structures, the loading rates are set to 0.84 mm/min and 1.68 mm/min, respectively. Force and displacement data are obtained respectively by the force sensor and the displacement sensor. The Daheng industrial camera is employed to capture the deformation process of the structure during testing, with the frame rate set to one frame per second to ensure continuous recording of structural deformation changes.

S3.2 Quasi-static compression simulation

The numerical simulations of quasi-static compression were conducted using the explicit dynamic module (with nonlinearity enabled) of ABAQUS 2022. Two rigid shells were placed at the top and bottom of the structure to simulate the upper pressing head and lower plate in the experiment. A constant displacement boundary condition

was applied to the upper plate to simulate constant-speed compression. To balance calculation efficiency while avoiding dynamic inertia effects, the velocity was set to 100 mm/s. No tie was applied between the components, and only contact interactions were considered. The solid mesh C3D8R was used for the finite element modeling of each component. After performing grid convergence analysis, the mesh sizes for the PRM and LB components were set to 0.25 mm, while the mesh size for the assemble panel was set to 0.75 mm. The elastic modulus, density, Poisson's ratio, and the JC model parameters (excluding the strain rate parameter c) of Al6061 are used as material properties in the model, as shown in Table 1. Normal contact is set to hard contact, tangential contact is set to penalty method with the factor is set to 0.15.

S3.3 Energy absorption performance

In general, the crashworthiness indicators of structures include energy absorption (*EA*), specific energy absorption (*SEA*), effectiveness of energy absorption (*EEA*) and load-carrying capacity (*ULC*), the coefficient of variation of the plateau stress standard deviation (CV_{ps}). The initial yield force is the force value corresponding to the starting point of inelastic deformation when the structural deformation exceeds the elastic limit. The calculation equation of strain is as follows,

$$\varepsilon = \frac{\Delta l}{L} \tag{7}$$

where, Δl denotes the deformation of the structure in the target direction, while L represents the initial geometric length in that same direction.

Energy absorption (*EA*) represents the total energy absorbed by the internal structure under effective compression deformation, and its mathematical expression is

$$EA = \int_0^{S_{cE}} F(s)\mathrm{d}s \tag{8}$$

where $F(s)$ is the crushing force as a function of the compression deformation s, S_{cE} is the effective stroke displacement, representing the critical point at which the structure enters densification. The S_{cE} is related to the peak inflection point of the energy absorption efficiency (*EAE*). The mathematical expression of *EAE* is as follows

$$EAE = \frac{\int_0^{S_c} F(s)\mathrm{d}s}{F_{\max}} \tag{9}$$

where S_c is the compression displacement, F_{max} is the peak force within 0 to s except for the initial peak load. The value of the EAE often exhibits a trend of initially increasing and then decreasing with increasing compression displacement. The inflection point in this curve is identified as the onset of structural densification. Consequently, the corresponding displacement at this point is defined as S_{cE}.

Specific energy absorption (SEA) is an important indicator for evaluating the energy absorption performance per unit mass between different structures. The mathematically expressed of SEA is as follows

$$SEA = \frac{EA}{m} \tag{10}$$

where m is the core mass of the sandwich structure.

The effectiveness of energy absorption (EEA) is defined as the energy absorbed by the structure divided by the net volume of a structure and yield strength (σ_Y) of the material, which indicates when the whole structure has entered the plastic state. EEA is a dimensionless energy absorption indicator characterizing the volumetric efficiency of structures under compression. The mathematically expressed of SEA is as follows

$$EEA = \frac{EA}{V\sigma_Y} \tag{11}$$

where V is the core volume of the sandwich structure.

S3.4 Specific modulus and specific strength comparison

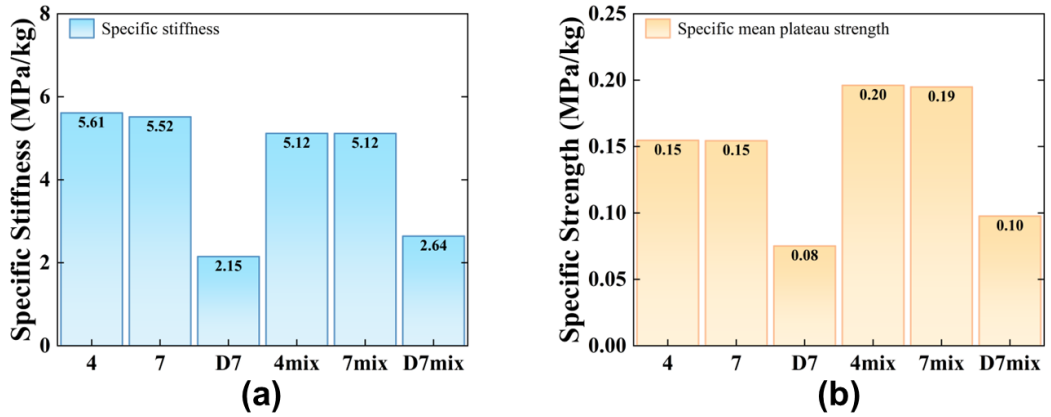

Figure S7 Comparison of (a) specific stiffness and (b) specific strength values for the six RMMM-structured sequences.

S3.5 Stress fluctuation comparison

The undulation of load-carrying capacity (*ULC*) is used to evaluate the stability of response force under the compressive process. The lower *ULC* of structures, the smoother their force response curves. The mathematical expression of *ULC* is as follows

$$ULC = \frac{\int_0^{S_{cE}} \left| F(s) - MCF \right| \mathrm{d}s}{\int_0^{S_{cE}} F(s) \mathrm{d}s} \tag{12}$$

where *MCF* is the mean crushing force, represents the average load-carrying level of the structure during the effective compress stroke. The calculation equation of *MCF* is as follows,

$$MCF = \frac{EA}{S_{cE}} \tag{13}$$

The coefficient of variation of the plateau stress standard deviation (CV_{ps}) is used to characterize the volatility of the local stress plateau segments during the compression process of the structure. The mathematical expression of CV_{ps} is as follows

$$CV_{ps} = \frac{\sigma_{sd}}{\bar{\sigma}} \tag{14}$$

$$\sigma_{sd} = \sqrt{\frac{1}{N} \sum_{i=1}^{N} \left(\sigma_i - \bar{\sigma} \right)^2} \tag{15}$$

where the σ_{sd} is standard deviation of stress plateau section, $\bar{\sigma}$ is the mean plateau stress, and σ_i is the stress value of the *i*-th point in the plateau section.

Figures 3D-F compare the stress wave characteristics of RMMM structures with those of existing modular metamaterials. The control group structures include origami-based self-locking system[2], interlocking modular metamaterials[3], modular auxetic structures[4] and assembled re-entrant honeycomb structure[5], with their stress-strain curves shown in Figure S8. The first dotted line marks the beginning of the stress plateau section, while the second dotted line indicates the end of the plateau and the critical strain point at which densification begins. The manufacturing method and materials of the control group structures are shown in Tasble S3.

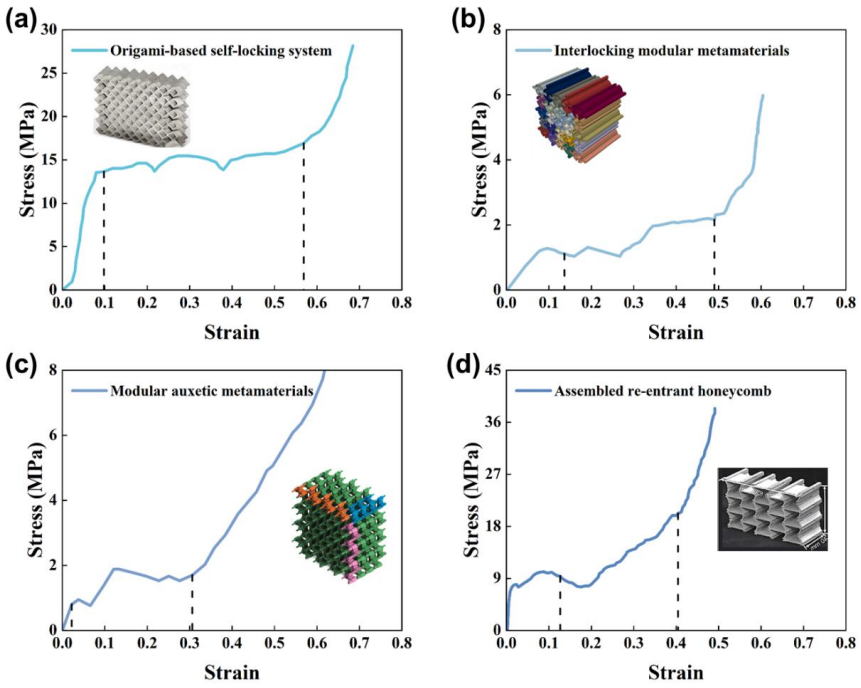

Figure S8 The quasi-static compression stress-strain curves of (a) origami-based self-locking system[2], (b) interlocking modular metamaterials[3], (c) modular auxetic structures[4] and (d) assembled re-entrant honeycomb structures[5]

Table S3 Manufacturing method and material of the modular metamaterials

Structures	Materials	Manufacturing method	Material model	Structural fracture
RMMM (this study)	6061 aluminums	SLM 3D-printing	Johnson–Cook plasticity model	No
Origami-based self-locking system[2]	316L stainless steel	SLM 3D-printing	Bilinear constitutive model	No
Interlocking modular metamaterials[3]	316L stainless steel	SLM 3D-printing	Bilinear constitutive model	No
Modular auxetic structures[4]	316L stainless steel	SLM 3D-printing	Bilinear constitutive model	No

Assembled re-entrant honeycomb structures[5]	316L stainless steel	SLM 3D-printing	true stress–strain curve combined with the ductile damage model	No

S3.6 Ashby figure comparison

Figure 3G-H present Ashby plots of specific energy absorption (*SEA*) and effectiveness of energy absorption (*EEA*) versus relative density, allowing for a comparative analysis of the energy absorption performance between different modular metamaterials. The relative density ρ^* is a dimensionless parameter used to characterize the lightweight of structures, and its mathematical expression is given by:

$$\rho^* = \frac{m}{\rho V} \tag{16}$$

where m is the mass of the structure, ρ is the density of the base material in Table S1 and V is the space volume occupied by the structure.

S4 Drop-weight impact test and simulation

S4.1 Drop-weight impact test

The dynamic protective performance of modular metamaterials is evaluated using an Instron drop impact tester, as shown in Figure S9. The impactor consisted of a circular steel hammer with a diameter of 100 mm and a base weight of 7 kg. Its impact mass can be adjusted by adding weights to a box mounted above the hammer. Force response data are collected via a force sensor positioned above the hammer. Structural deformation during impact is captured using a nac MEMRECAM ACS-3 M16 High Speed Camera. To track the displacement of the hammer, a patch of artificial speckle pattern is applied to its front surface, and displacement data were extracted from the deformation images using Digital Image Correlation (DIC) technology.

S4.2 Drop-weight impact simulation

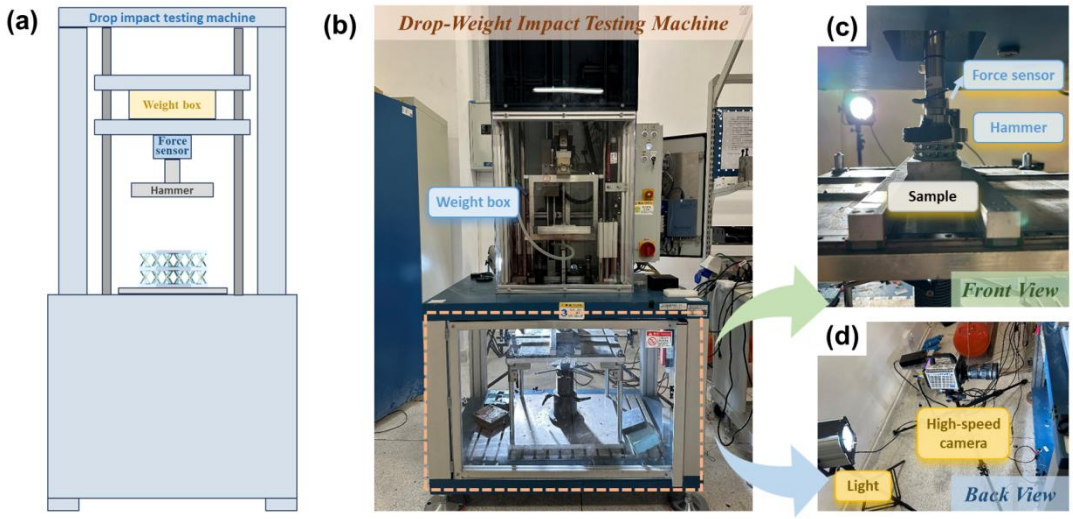

Figure S9 (a) Schematic diagram of drop-weight impact tests; (b-d) Diagram of the drop hammer impact testing.

In the dynamic impact simulation, a discrete rigid circle shell with a diameter of 10 mm is adopted as the plate hammer. Apply the hammer mass and the initial predefined impact velocity at the central reference point of the rigid shell. In addition, a gravity force corresponding to the weight of the hammer is also applied at the central reference point and guides downward to supplement the gravity effect of the hammer in the actual impact event. The reference point of the hammer is set with all degrees of freedom fixed except for the impact direction, corresponding to the motion mode of the hammer facility of the drop impact testing machine. The material model employs JC parameters with strain rate, and the meshing and other settings are consistent with those used in the quasi-static compression simulation. Meanwhile, the contact force between the discrete rigid shell and the upper surface of the specimen is extracted as the control data with the test response force.

S4.3 Force-time curves under the same impact energy but with different impact masses

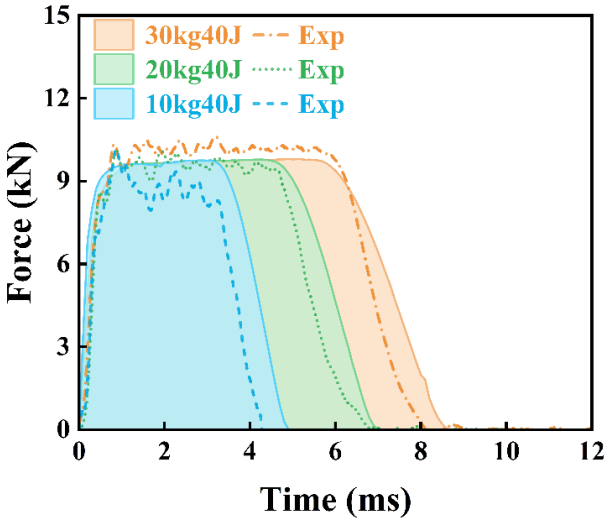

Figure S10 The impact force-time curves at the impact mass of (a) 10kg, (b) 20kg and (c) 30kg.

Figure S10 shows the force-time curves of the RMMM-7mix structure at an impact energy of 40J with varying impact masses. The dotted line represents experimental data, while the solid line represents simulation data. Both sets of data are relatively consistent across different mass values. When the impact energy remains constant, the peak force does not change significantly with increasing mass. However, the duration of the impact process increases noticeably, which could be attributed to the enhanced inertia effect of the hammerhead as mass increases.

S5 PFKAN-LSTM Deep Learning Prediction Model

S5.1 Kolmogorov-Arnold Network

The principle of the KAN network is inspired by the Kolmogorov-Arnold theorem, proposed by Vladimir Arnold and Andrey Kolmogorov. The theorem states that if $f(x)$ is a multivariate continuous function defined on a bounded domain, then $f(x)$ can be expressed as a finite composition of continuous functions of a single variable, combined using the binary operation of addition. Therefore, for a two-layer KAN network with shape [n, $2n$+1, 1], its structure is shown in Fig.5f, and its mathematical expression is as follows[6]:

$$f(x)=f(x_1,\cdots,x_n)=\sum_{q=1}^{2n+1}\Phi_q\left[\sum_{p=1}^{n}\phi_{q,p}(x_p)\right] \tag{17}$$

where, $\phi_{q,p}$ represents the first layer function (from the input layer to the hidden layer), ϕ_q represents the second layer function (from the hidden layer to the output layer). They

are both one-dimensional functions with trainable parameters. In this work, these one-dimensional functions are parameterized as B-spline basis functions.

$$\phi_{q,p}(x) = \sum_{k=1}^{K} c_{q,p}^{(k)} B_k(x) \tag{18}$$

Where $c^k_{q,p}$ is trainable parameter, $B_k(x)$ is B-spline function. The use of B-spline basis functions allows for greater flexibility in modeling complex relationships between input features, and their smooth, piecewise-defined nature makes them ideal for capturing the nonlinearities in the data, which is particularly beneficial for dynamic systems like impact response curves.

S5.2 Long Short-Term Memory

Long Short-Term Memory (LSTM), proposed by Hochreiter and Schmidhuber in 1997[7], features a memory cell that spans the entire sequence, carrying long-term memory information. This unique structure allows LSTM to perform exceptionally well in tasks involving time series data and long-range dependencies. The LSTM structure is shown in Fig.5f, its working principle can be explained using the following equations[8]:

$$f_t = \sigma\left[W_f\left(x_t, h_{t-1}\right) + b_f\right] \tag{19}$$

$$i_t = \sigma\left[W_i\left(x_t, h_{t-1}\right) + b_i\right] \tag{20}$$

$$g_t = \tanh\left[W_c\left(x_t, h_{t-1}\right) + b_c\right] \tag{21}$$

$$c_t = \sigma * c_{t-1} + i * g_t \tag{22}$$

$$o_t = \sigma\left[W_o\left(x_t, h_{t-1}\right) + b_o\right] \tag{23}$$

$$h_t = o_t * \tanh\left(c_t\right) \tag{24}$$

where, the W_f, W_i, W_c, and W_o represent the weights for the forget gate, input gate, output gate, and block input, respectively. The b_f, b_i, b_c, and b_o represent the corresponding biases. And the σ is the sigmoid activation function, and $tanh$ is also an activation function.

S5.3 Smooth L1 loss

Smooth L1 Loss was originally proposed in Fast R-CNN to make bounding box regression more robust by replacing the excessively strict L2 Loss [9, 10]. In Smooth L1

Loss described in Eq.(25), a point β splits the positive axis range into two parts: L2 loss is used for targets in range [0,β], and L1 loss is used beyond β to avoid over-penalizing outliers. Here, β is set to 0.5.

$$f(x)=\begin{cases} 0.5\dfrac{x^2}{\beta}, & if\ |x|<\beta \\ |x|-0.5\beta, & otherwise \end{cases} \tag{25}$$

Where, x presents the predicted value.

S5.4 Evaluation metrics

The Coefficient of Determination R^2 is a statistical metric that explains how well the predictions of a model fit the real data.

$$R^2=1-\frac{\sum_{i=1}^{n}\left[f(x_i)-y_i\right]^2}{\sum_{i=1}^{n}\left[f(x_i)-\bar{y}\right]^2} \tag{26}$$

Where $f(x_i)$ is the predicted value, y_i is the real value, $\bar{y}$ is the mean of actual values and n is the number of data points.

Mean absolute error (MAE) measures the average magnitude of absolute errors in a set of predictions, without considering their direction (positive or negative).

$$MAE=\frac{1}{n}\sum_{i=1}^{n}\left|f(x_i)-y_i\right| \tag{27}$$

Mean squared error (MSE) measures the average squared difference between the actual and predicted values, and it indeed places more emphasis on larger errors compared to MAE.

$$MSE=\frac{1}{n}\sum_{i=1}^{n}\left[f(x_i)-y_i\right]^2 \tag{28}$$

Root mean squared error (RMSE) is the square root of MSE. It gives a sense of the magnitude of error in the same units as the target variable.

$$RMSE=\sqrt{MSE} \tag{29}$$

Reference

[1] Johnson, G.R. and Cook, W.H. A Constitutive Model and Data for Metals Subjected to Large Strains, High Strain Rates, and High Temperatures., *Proceedings of the 7th International Symposium on Ballistics*, The Hague, 19-21 April 1983, 541-547.

[2] Chen Z, Wei X, Yang L, et al. Origami-based bidirectional self-locking system for energy absorption. *Journal of the Mechanics and Physics of Solids*, 2024, 188: 105672.

[3] Li J, Sui C, Sang Y, et al. A flexible, reusable and adjustable high-performance energy absorption system inspired by interlocking suture structures. *International Journal of Solids and Structures*, 2024, 296: 112839.

[4] Li Z, Zhu Y, Yang K. Modular metamaterials with strong auxeticity, tunability and crashworthiness. *International Journal of Solids and Structures*, 2025: 113577.

[5] Lang J P, Jiang W, Teng X C, et al. Assembled mechanical metamaterials with transformable shape and auxeticity. *Construction and Building Materials*, 2023, 378: 131181.

[6] Liu Z, Wang Y, Vaidya S, et al. Kan: Kolmogorov-arnold networks. *arXiv preprint* arXiv:2404.19756, 2024.

[7] Sepp Hochreiter, Jürgen Schmidhuber; Long Short-Term Memory. *Neural Comput* 1997; 9 (8): 1735–1780.

[8] Van Houdt G, Mosquera C, Nápoles G. A review on the long short-term memory model. *Artificial intelligence review*, 2020, 53(8): 5929-5955.

[9] Girshick R. Fast r-cnn, *Proceedings of the IEEE international conference on computer vision*. 2015: 1440-1448.

[10] Fu C Y, Shvets M, Berg A C. RetinaMask: Learning to predict masks improves state-of-the-art single-shot detection for free. *arXiv preprint,* arXiv:1901.03353, 2019.